3D PIC simulations of collisionless shocks at lunar magnetic anomalies and their role in forming lunar swirls

R. A. Bamford, E. P. Alves, F. Cruz, B. J. Kellett, R. A. Fonseca, L. O Silva, R. M. G. M. Trines, J. S. Halekas, G. Kramer, E. Harnett, R. A. Cairns, and R. Bingham

Published version information:

Citation: Bamford, RA et al. "3D PIC simulations of collisionless shocks at lunar magnetic anomalies and their role in forming lunar swirls." Astrophysical Journal, vol. 830, no. 2 (2016): 146.

doi: 10.3847/0004-637X/830/2/146

The Astrophysical Journal, 830:146 (12pp), 2016 October 20 doi:10.3847/0004-637X/830/2/146

3D PIC SIMULATIONS OF COLLISIONLESS SHOCKS AT LUNAR MAGNETIC ANOMALIES AND THEIR ROLE IN FORMING LUNAR SWIRLS

R. A. Bamford[1], E. P. Alves[2], F. Cruz[2], B. J. Kellett[1], R. A. Fonseca[3], L. O Silva[2], R. M. G. M. Trines[4], J. S. Halekas[5], G. Kramer[6], E. Harnett[7], R. A. Cairns[8], and R. Bingham[9,10]

[1] RAL Space, STFC, Rutherford Appleton Laboratory, Chilton, Didcot, OX11 0QX, UK; Ruth.Bamford@stfc.ac.uk
[2] GoLP/Instituto de Plasmas e Fusão Nuclear, Instituto Superior Técnico, Universidade de Lisboa, 1049-001 Lisbon, Portugal
[3] DCTI/ISCTE—Instituto Universitário de Lisboa, 1649-026 Lisbon, Portugal
[4] Central Laser Facility, STFC, Rutherford Appleton Laboratory, Chilton, Didcot, OX11 0QX, UK
[5] Department of Physics and Astronomy, 414 Van Allen Hall, University of Iowa, Iowa City, IA 52242, USA
[6] The Lunar and Planetary Institute, USRA, 3600 Bay Area Blvd, Houston, TX 77058, USA
[7] Department of Earth and Space Science, University of Washington, Seattle, WA 98195-1310, USA
[8] University of St Andrews, North Haugh, St. Andrews, Fife, KY16 9SS, UK
[9] SUPA, University of Strathclyde, Glasgow, Scotland, 4G 0NG, UK
Received 2015 October 20; revised 2016 June 30; accepted 2016 July 16; published 2016 October 18

ABSTRACT

Investigation of the lunar crustal magnetic anomalies offers a comprehensive long-term data set of observations of small-scale magnetic fields and their interaction with the solar wind. In this paper a review of the observations of lunar mini-magnetospheres is compared quantifiably with theoretical kinetic-scale plasma physics and 3D particle-in-cell simulations. The aim of this paper is to provide a complete picture of all the aspects of the phenomena and to show how the observations from all the different and international missions interrelate. The analysis shows that the simulations are consistent with the formation of miniature (smaller than the ion Larmor orbit) collisionless shocks and miniature magnetospheric cavities, which has not been demonstrated previously. The simulations reproduce the finesse and form of the differential proton patterns that are believed to be responsible for the creation of both the "lunar swirls" and "dark lanes." Using a mature plasma physics code like OSIRIS allows us, for the first time, to make a side-by-side comparison between model and space observations. This is shown for all of the key plasma parameters observed to date by spacecraft, including the spectral imaging data of the lunar swirls. The analysis of miniature magnetic structures offers insight into multi-scale mechanisms and kinetic-scale aspects of planetary magnetospheres.

Key words: acceleration of particles – Moon – magnetic fields – planets and satellites: magnetic fields – plasmas – shock waves

1. INTRODUCTION

The Moon does not have an active core dynamo with which to generate its own global magnetic field (Lyon et al. 1967). It does, however, have several small, static regions of low magnetic field ($\sim$50–500nT) on the surface (Dyal et al. 1970; Coleman et al. 1972). The distribution of these magnetic field anomalies on the Moon varies from thousands of kilometers across, irregular conglomerations and clusters, to relatively small (hundreds of kilometers across) and isolated features—such as the Reiner Gamma formation and Gerasimovich magnetic anomaly (Hood & Schubert 1980; Halekas et al. 2001; Richmond et al. 2003; Hood & Artemieva 2008). The largest distributions of crustal magnetic anomalies are located on the southern part of the far side of the Moon, antipodal to the Crisium, Serenitatis, Imbrium, and Orientale basins (Hood & Schubert 1980; Halekas et al. 2001; Richmond et al. 2003; Hood & Artemieva 2008). The presence of small areas of magnetic field on an otherwise unmagnetized planetary body is not unique to the Moon. Mars, Mercury, and some asteroids are known to also possess small-scale magnetic fields (Kivelson et al. 1995; Acuna et al. 1999; Starukhina & Shkuratov 2004).

Figure 1 shows a graphical summary of the in situ observations from spacecraft that intersected the mini-magnetospheres that were formed as a result of the solar wind interacting with the magnetic anomalies on the Moon's surface. The computational investigation into mini-magnetospheres has become an area of considerable interest. A number of papers on hybrid (Bamford et al. 2008; Gargaté et al. 2008; Kallio et al. 2012; Poppe et al. 2012) and particle-in-cell (PIC) (Kallio et al. 2012; Bamford et al. 2013a, 2013b, 2015; Deca et al. 2014, 2015; Jarvinen et al. 2014; Cruz et al. 2015, 2016; Dyadechkin et al. 2015; Fatemi et al. 2015) simulations have been authored, following from previous magnetohydrodynamic (MHD) simulations (Harnett & Winglee 2002, 2003; Kurata et al. 2005). Here we perform fully self-consistent PIC simulations in 2D and 3D, with a realistic proton-to-electron mass ratio. This provides, for the first time, a direct comparison between theory and observational signatures for a small (sub-ion Larmor radius), isolated magnetic anomaly forming a collisionless shock.

We have reproduced all the major observational characteristics of lunar swirls, using the simplest of magnetic topologies—a single dipole, under a variety of orientations and solar wind conditions. Low beta, magnetized solar wind flows with Alfvèn Mach numbers between 2 and 8 are used here, consistent with the formation of laminar and turbulent quasi-perpendicular collisionless shocks studied by numerical methods for planetary magnetospheres (e.g., Forslund & Freidberg 1971; Forslund et al. 1984; Blandford & Eichler 1987; Quest 1988; Kucharek & Scholer 1995).

[10] Also at Central Laser Facility, STFC, Rutherford Appleton Laboratory, Chilton, Didcot, OX11 0QX, UK.

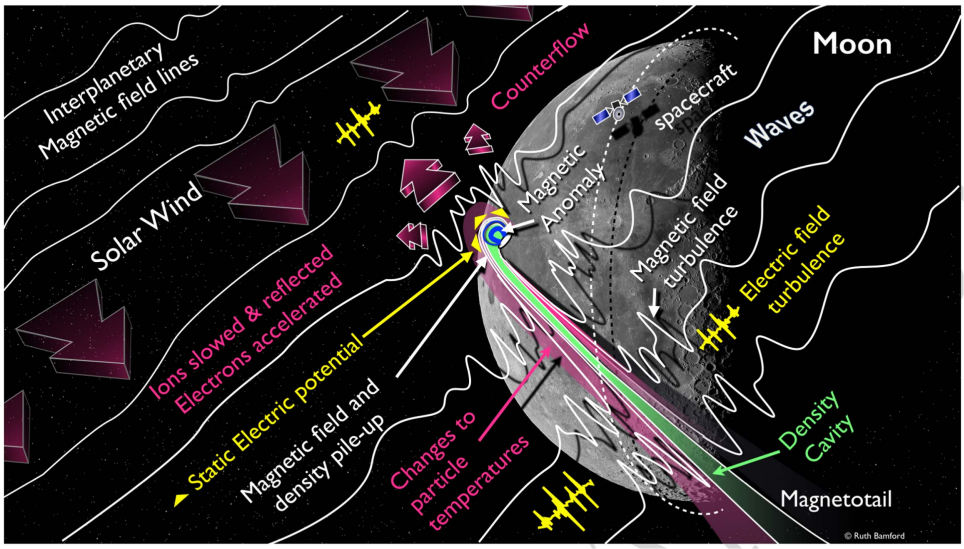

Figure 1. A graphical summary of the spacecraft observational data (Lin et al. 1998; Huixian et al. 2005; Wieser et al. 2009, 2010; Futaana et al. 2010; Hashimoto et al. 2010; Lue et al. 2011; Wang et al. 2012; Halekas et al. 2014; Yokota et al. 2014) of Lunar mini-magnetospheres. The solar wind plasma with an embedded magnetic field, encounters the small (∼10–100 km) crustal magnetic field (∼400nT) on the lunar surface, producing a "mini-magnetosphere." The mean value of the solar wind magnetosonic Mach number is $M_{\rm m} = 8$ (Edberg et al. 2010), with a $\beta = 0.2$. A shock-like discontinuity in density and magnetic field can occur as low as ∼10–20 km above the surface (Halekas et al. 2014) and with a magnetotail that is drawn out into space by 10,000s km (Futaana et al. 2010). The width of the barrier region is very narrow, ∼1–20 km. Within the barrier, plasma is less turbulent within the diamagnetic cavity, and much of the incoming proton density has been excluded (Wieser et al. 2010). Upstream of the narrow interface region, however, increased levels of magnetic and electrostatic turbulence, including Whistlers-modes (Halekas et al. 2006; Nakagawa et al. 2011), are observed, with waves occurring at or near the local lower-hybrid plasma frequency and Alfvén waves (Saito et al. 2012). The source of the turbulence and waves, counter-streaming protons, is reflected back by the magnetic boundary. The observations of the plasma particle distributions show a slowing and reversing of the flow of the protons, accompanied by a cooling upon approaching the magnetopause. Conversely, the electrons experience an acceleration toward the anomaly and heating across the transition (Saito et al. 2012). The simultaneous accelerations and deaccelerations of opposite charges imply the existence of a sizeable (≈100–400 V m^{-1}), static electric field pointing anti-Moonward above the magnetic anomaly site (Saito et al. 2012). The changes in temperature indicate a non-adiabatic dissipative interaction between solar wind protons and lunar magnetic anomalies.

In this paper we review the observational data taken by all spacecraft to date. This is compared with results from a PIC code providing a one-to-one correspondence. Figure 1 shows a summary of the accumulated observations.

The simulations quantifiably confirm the satellite (Halekas et al. 2014) findings and the theoretical predictions (Bamford et al. 2012), namely that a miniature collisionless shock can be responsible for all the observations (Lin et al. 1998; Huixian et al. 2005; Wieser et al. 2009, 2010; Futaana et al. 2010; Hashimoto et al. 2010; Lue et al. 2011; Wang et al. 2012; Halekas et al. 2014; Yokota et al. 2014). Here it is confirmed that the interaction or boundary layer can form well above (i.e., kilometers rather than meters) the lunar surface (depending upon conditions) and need not be a photoelectricsheath (Garrick-Bethell et al. 2011) restricted to a few meters above the surface. A 2D parametric analysis of dipole characteristics illustrates how the primary driving term for generating the electric field is the gradient in energy density, therefore it is not exclusive to one magnetic field orientation or magnetic mirroring. Asymmetries appear in the diamagnetic cavity due to differences in the preferred plasma instabilities, their growth, and interchange rates. The parametric analysis also shows how observational verification of the formation of the very smallest mini-magnetospheres and collisionless shocks may be very difficult to determine due to the relative spacecraft speed and dipole size.

The analysis of mini-magnetospheres is very interesting for fundamental plasma physics. Their occurrence in space means that non-intrusive measurements are possible, including particle distribution functions. The fact that they are located on our nearest planetary body also provides a high level of diverse observational data.

Of particular astronomical interest is the apparent link between the mini-magnetospheres and the "lunar swirl" patterns on the Moon (El-Baz 1972; Hood & Schubert 1980; Hood & Williams 1989; Blewett et al. 2011). The analysis here shows how the fine structure observed within the swirls, as well as the narrow enhanced "dark lanes," can be reproduced by the fine-scale plasma interactions at the same approximate dimensions and magnetic field strengths.

2. LUNAR SWIRLS AND MAGNETIC ANOMALIES

Lunar swirls are optically distinct, white surface features that are found in several locations across the Moon's surface (El-Baz et al. 1972). The features are distinctive due to their fluid or wispy structure that is unlike either craters or impact ejecta. Their form has been determined to be unrelated to geographical topography and appears to overprint on both mountainous and plateau terrains (Bell & Hawke 1987; Pinet et al. 2000; Blewett et al. 2007). Although not all magnetic field anomalies have identifiable lunar swirl patterns, no lunar swirls have been found that are not coincident with similarly sized areas of anomalous crustal magnetic field (Blewett et al. 2007; Kramer et al. 2011a).

Several theories exist to explain the creation of lunar swirls (Schultz et al. 1980; Starukhina & Shkuratov 2004; Garrick-Bethell et al. 2011). Recent work (Glotch et al. 2015; Harnett & Kramer 2015) on spectral data from the Diviner Lunar Radiometer on the *Lunar Reconnaissance Orbiter*, the Moon Mineralogy Mapper on board *Chandrayaan-1* (Kramer et al.

2011a), and spectrometer data from Clementine (Blewett et al. 2007; Richmond & Hood 2008; Kramer et al. 2011b) strongly support the hypothesis that the mechanism of the variations in albedo is related to differential solar wind/magnetospheric proton bombardment of the lunar regolith.

Proton bombardment reddens (darkens) the lunar regolith over time (Pieters et al. 1993). Persistent reduced proton flux leads to a "lighter" color, while extra enhanced proton flux leads to an even "darker" appearance. The interplay between the two results in "white wisps" interspersed with narrow "dark lanes" (Blewett et al. 2007; Richmond & Hood 2008; Kramer et al. 2011a; Glotch et al. 2015; Harnett & Kramer 2015).

These spectroscopic data mean that the lunar swirls are the first diagnostic observation directly linked to the interaction of the solar wind with the mini-magnetosphere above and onto the lunar surface. The interaction causes deflection of solar wind protons away from the "on-swirl" (Kramer et al. 2011a) surfaces and focuses them onto "off-swirl" (Kramer et al. 2011a) surfaces. The additional concentration of protons onto the narrow "dark lanes" (Blewett et al. 2007) enhances the spectral darkening effects of space weathering significantly, relative to normal lunar surfaces.

The formation and retention of the level of detail visible in the swirls requires a very precise and semi-consistent redirection of proton flux. The finesse of the transitions seen in the swirls (sometimes less than 1 km) further suggests that the process close (0–10s km) to the surface is tightly held by the magnetic footprint. A large-scale, remote plasma structure would be shifted and dispersed by the fluctuations in the solar wind and lunar cycle and the effects of transitions in and out of the regions of the Earth's magnetosphere; these cycles are likely to be the cause of the "wispiness" of swirls.

3. THE SIGNIFICANCE OF THE SCALE SIZE OF MAGNETIC ANOMALIES

The overall size of an isolated magnetic anomaly like the Gerasimovich magnetic anomaly is of the order of, or smaller than, the interplanetary plasma proton Larmor (gyro) radius $r_{\rm Li}$ in the interplanetary magnetic field ($B_{\rm IMF}$). For example, $r_{\rm Li} \sim 500$ km for a 450 km s^{-1} proton in a $B = 10nT$. However, the finesse of the details within the swirls suggests a level of detailed plasma interaction that is well below that of the proton dynamics scale.

This is quantified by determining the characteristic scale length of the magnetic inhomogeneity/magnetic anomaly $\tilde{\lambda}_B = [(1/B)(dB/dh)]^{-1}$. Here $\tilde{\lambda}_B$ vertically is ~20 km, assuming a surface magnetic field B of $200nT$ and the boundary to be at an altitude, h, of ~20 km, or horizontally ~70–300 km for the central region of Reiner Gamma (https://the-moon.wikispaces.com/Reiner+Gamma)

This means that the protons are effectively unmagnetized (Langmuir 1929).

Conversely, the electrons' gyro radii are small compared to the overall size of the structure in which they are able to follow the abrupt changes in magnetic field created by the solar wind interacting with the magnetic anomaly and diamagnetic cavity. The difference in behavior between the magnetized electrons and unmagnetized protons sets up a space-charge electric field that controls the protons' behavior (Bingham 1993; Borisov & Mall 2003). This occurs not just at the lunar surface but throughout the mini-magnetosphere boundary. In order to model this scale of interaction, these criteria must be maintained between lunar, laboratory (Bamford et al. 2008, 2012), and computer simulation,. Only a full plasma kinetic code (Dawson 1983; Fonseca et al. 2002) can capture these characteristics.

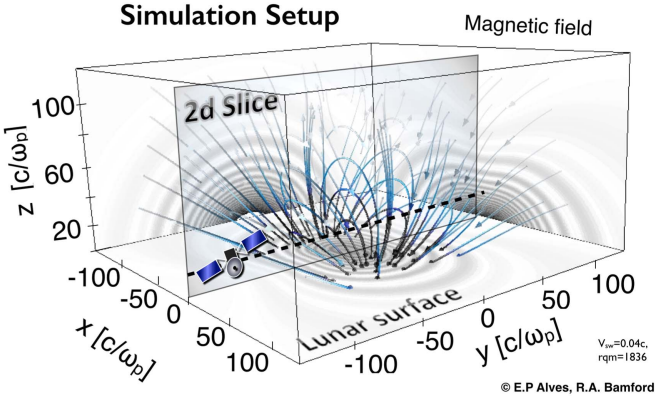

Figure 2. Geometry of the simulation. The lunar surface is represented by the lower $x-z$ plane. A single source magnetic dipole is placed just below and parallel to the $x-z$ plane, with the magnetic axis aligned along $x = 0$, with the north pole orientated in the $+z$ direction. The result is a hemispherical magnetic field emerging from the surface. The magnetic field intensity is shown projected onto the back walls and the ground plane is banded gray, where decreasing band interval corresponds to increasing magnetic field intensity. A magnetized "solar wind" plasma with density $n_{\rm sw}$ and magnetic field $B_{\rm sw}$ (anti-parallel to the anomaly field) is introduced from the top plane with a flow velocity $-\boldsymbol{v}_{\rm sw}$ vertically down onto the lunar surface. Selected magnetic field lines are shown in graduated blue. The magnetic dipole moment $\boldsymbol{m}_{\rm m}$ is 25 normalized units long and resides 25 units below the center of the box aligned with the positive $\boldsymbol{x}$-axis. The plane marked "2D slice" shows the relative orientation of the sections shown in Figure 4(a). The dashed line in the 2D section represents the path of a conceptual spacecraft sampling the parameters results that are shown in Figures 4(b) and 6(a). The simulation code operates in normalized plasma units with $n_{\rm sw}$ as the independent variable. The proton-to-electron charge-to-mass ratio used is the realistic value of 1836.

4. THE SIMULATIONS

The simulation was carried out using a plasma PIC code (Dawson 1983) called OSIRIS (Fonseca et al. 2002). In the OSIRIS code the full set of Maxwell's equations is solved on a grid using currents and charge densities calculated by weighting discrete particles onto the grid. Each particle is pushed to a new position and momentum via self-consistently calculated fields. The code makes few physics approximations and is ideally suited for studying complex systems with many degrees of freedom such as this one. The reason this is necessary is that the scale size of the mini-magnetosphere structure is much smaller than what the (MHD) code allows. No filtering is performed in these simulations. This allows us to resolve plasma waves in space and time, including whistler waves (Halekas et al. 2006; Nakagawa et al. 2011). The code is a time and space domain code, not a spectral code, so the equations are integrated via fast Fourier transforms.

The simulation setup is shown in Figure 2, together with a dipole field whose axis is parallel to the plane of the surface. Full 3D simulations result in Figure 3, which shows the magnetic field structure, the electric field, and proton orbits self-consistently derived.

Table 1 shows a summary of the 3D simulation parameters used and their relationship to typical observational values (based on Edberg et al. 2010).

In order to maintain dynamic similarity (Lacina 1971; Connor 1988; Ryutov et al. 2000) with the lunar environment,

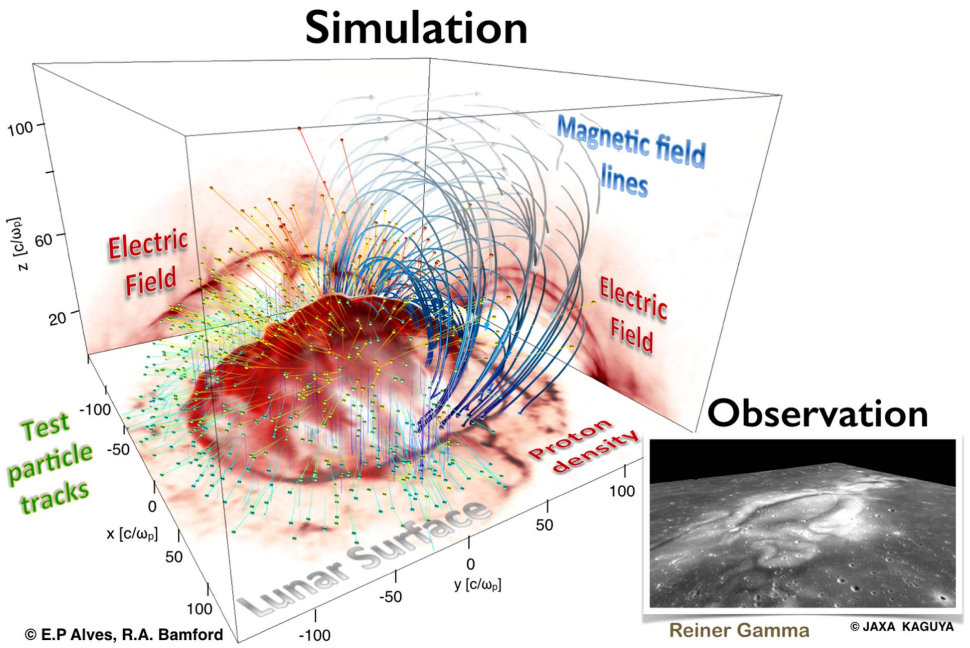

Figure 3. A 3D magnetized plasma collision with a surface magnetic dipole. Insert: a low-altitude, inclined angle photograph taken by the JAXA *Kaguya* (Kato et al. 2010) spacecraft of the Reiner Gamma Formation (https://the-moon.wikispaces.com/Reiner+Gamma) as an example of a lunar swirl albedo anomaly located coincident with a localized crustal magnetic field. The solar wind plasma (flowing vertically downward) impacts a localized crustal magnetic field structure (blue lines). The green spheres and tracks show a subset of the protons' population trajectory being scattered from the narrow polarization electric field (red). Proton density enhancements follow the electric field. Only part of the magnetic field lines are shown for clarity and the background densities are not visualized. Superficial similarities of form and "wisp-like" structures in the lunar swirl pattern are present, such as the pattern of the proton (red) deposition on the surface plane in the simulation.

Table 1
A Table of the Plasma Parameter Values Used in the 3D Simulation

Plasma Parameter	Symbol	Value
Plasma temperature	T_i	5 eV
Plasma sensitivity	$n_{\rm sw}$	10 cm^{-3}
Solar wind flow velocity[a]	$v_{\rm sw}$	600 s^{-1}
Solar wind magnetic field[a]	$B_{\rm sw}$	$10nT$
Debye length	λ_D	0.01 km
Thermal proton Larmor orbit	$r_{L,i,\rm th}$	97 km
Flow proton Larmor orbit	$r_{L,i,\rm fl}$	627 km
Electron Larmor radius	r_{Le}	1 km
Electron skin depth	c/ω_{pe}	1.7 km
Ion skin depth	c/ω_{pi}	97 km
Magnetic field at standoff[a]	$\lvert B(r_s)\rvert$	$120nT$
Magnetosonic mach	M_m	8
Plasma beta	β	0.2
Ratio ion-electron charge-to-mass	rqm	1836
Simulation box size		340 × 340 × 170 km
Grid resolution		300 m

Note.
[a] Operationally, for computational speed plasma inflow and source magnetic field, both increase by a factor of $F = 20$, which maintained pressure balance $B^2/2\mu_o = n_{\rm sw} m v_{\rm sw}^2/2$ at a standoff altitude of $r_s = c/\omega_{pi}$.

the magnetic fields and temperatures were normalized proportionately to maintain the same control variables of plasma β (thermal pressure to magnetic pressure) and M_m (magnetosonic mach numbers and speeds).

The simulation code is used here to recreate simplified case study combinations of plasma parameter conditions and magnetic field dipole orientations and intensities. These can be compared to the analytical expressions (Bamford et al. 2012) and observational data, e.g., Halekas et al. (2014), for mini-magnetospheres.

Figure 3 shows the results of the simulation of the solar wind plasma impacting a localized crustal magnetic field structure. The insert is a photograph of the Reiner Gamma lunar swirl taken by the *Kaguya* (Kato et al. 2010) spacecraft. This particular image is at an inclined angle similar to the simulation image's orientation to the representative plane of the "lunar surface," allowing a comparison of the footprint deposition of protons (red) in the simulation and the "white" of the lunar swirl.

In Figure 3 only the proton density above a threshold is visualized, in order to make the box transparent. The magnetic field structure is shown by the blue field lines (again in part omitted for the sake of clarity). The red line represents the magnitude of the space-charge electric field at the boundary, which is setup by the different penetration depths between protons and electrons at the edge of the magnetosphere. (Just the vertical (z) component of the electric field vector is shown in Figure 7). The lateral-projections of the electric field structure (which also correspond approximately to the peak concentration in the relative proton density), reveal interesting dynamic features and orthogonal asymmetries. The projection on the $y-z$ plane shows a rippled surface structure, due to the diamagnetic electron-ion drift instability that occurs perpendicular to the magnetic field lines (Cruz et al. 2015). In contrast, the projection on the $x-z$ plane shows a smooth surface structure, since the relative electron-ion drift is absent. This illustrates the anisotropic preferences of particular plasma instabilities. However, the narrow width of the barrier remains as a consistent feature, although it is not necessarily a single, smooth boundary, due to waves, turbulence, and instabilities—

the magnitude of which alters with specific conditions. Representative trajectories of a few solar wind protons are shown by the small spheres and yellow track lines and are seen to be widely scattered not by a gradual redirection, but rather are ballistically scattered from a very narrow region close to the surface. The electric field responsible for the scattering can be seen to be omnidirectionally pointing outward, regardless of the magnetic field orientation. This is because it is proportional to the *gradient* in the magnetic field intensity, $\nabla|B|^2$, not $|\boldsymbol{B}|$, in accordance with theoretical expectations (Bamford et al. 2012). The projection onto the $x-y$ or surface plane shows the electric field intensity at the lunar surface. The proton density is controlled, on these scales, by the electric field rather than the magnetic field because the protons are unmagnetized. The simulation shown in Figure 3 therefore shows the distribution of sharp regions of enhanced proton flux and regions of depleted proton flux.

4.1. 2D Cut-throughs of the 3D Simulation

In order to reveal the details of the interior structures of the 3D simulation Figure 4 shows the 2D sections of each of the plasma parameters. From top to bottom, these are the proton and electron density n_i, n_e, the resultant electric E, and the magnetic field B and the original dipole magnetic field undisturbed by the solar wind plasma $B_{\rm dipole}$. The plane of the section bisects the midpoint in x of the dipole axis and is indicated in Figure 2. Figure 4 shows the simulated plasma instrument signatures for the specific altitude ($20 \times c/\omega_{pe} = 34$ km for plasma density of 10 cm^{-3}) indicated in the previous Figures (4–9). Clearly, a flight path at different altitudes, orientations, and conditions will alter the plots (some of which will be shown later). However, this example from a single dipole contains all the basic component features of the double layers of the barrier going in and out of the cavity.

The density pile-ups, exclusion of the majority of the particles from the interior, backflow, and turbulence of the barrier are apparent with all parameters. The barrier that forms results in responsive inductive currents and corresponding magnetic fields. The thickness of the barrier is of the order of the electron skin depth $\sim c/\omega_{pe}$, as theoretically predicted by Bamford et al. (2012). The small-scale plasma instabilities, waves, and turbulence that are formed provide the means by which the proton and electron particle distributions become non-thermal and exchange energy through Landau damping (Bingham 1993). This is illustrated in Figure 4.

The "standoff" distance, r_s (Bamford et al. 2012), that the magnetic cavity reaches, forces a balance with the incoming plasma. For a cavity to be evident requires r_s to be greater than the barrier width/electron skin depth. Most important is the intensity of the magnetic field *at the magnetopause*. The placement of the reference "lunar surface" plane can go up or down, making reference to a surface magnetic field intensity that is dependent on the choice of distance from the magnetopause. These simulations show that a magnetic field intensity of $<300nT$ would be sufficient to produce a "mini-magnetosphere" for a density 10 cm^{-3}.

4.2. Simulating Spacecraft Flyover Signatures

Figure 4 shows how the simulation results translate to observations from a spacecraft flying above the surface anomaly.

These features should be common to any mini-magnetosphere to some degree or another, irrespective of the presence of lunar swirls. The comparison is qualitative rather than quantitative in order to highlight the nature of the interplay between the parameters, which should help to provide identification of the phenomena between theory and observations via simulation visualization.

4.3. Particle Distributions and Kinetic Instabilities

In a previous paper (Bamford et al. 2012), in situ satellite data, theory, and laboratory validation showed that it is an electric field associated with the small-scale collisionless shock that is responsible for reflecting, slowing, and deflecting the incoming solar wind around mini-magnetospheres. It was shown that the electric field of polarization, caused by the gradient in the magnetic field, between charge carriers of the solar wind flow, is of prime importance. This polarization field leads to reflection and scattering of the protons and electrons (Bingham et al. 2010). The counter-streaming of the protons ahead of the barrier is responsible for generating lower-hybrid waves via the modified two-stream instability (McBride et al. 1972). The electric potential component, ϕ, responsible for slowing and deflecting the protons (Bamford et al. 2012) is:

$$\phi = -(1/2\mu_0 ne).B_z^2.$$

For a density of ~ 5 cm^{-3} and a magnetic field, $B_z \sim 30 \times 10^{-9}T$ (similar to those observed at the pile-up reported by *Lunar Prospector*; Lin et al. 1998) provides a theoretical value of $\phi_{\rm theory} \sim 450$ V (Bamford et al. 2012), similar to the $\phi_{\rm obs} \sim 400$ V (Futaana et al. 2010). The value for these simulations for $n = 10$ cm^{-3} is $\delta E \approx 300$ V.

The plasma wave turbulence is identified to be close to the lower-hybrid frequency $= (\omega_{ce}\omega_{ci})^{1/2}$, where ω_{ce} and ω_{ci} are the electron and proton cyclotron frequencies respectively, agreeing with data from spacecraft that observed intense lower-hybrid electrostatic oscillations of the order of 1–10 Hz (Futaana et al. 2003). The lower-hybrid waves generated by the modified two-stream instability previously reported by Bingham et al. (2010), and shown to be responsible for the electron acceleration, are also observed by the satellites. These waves are also present at other collisionless shocks (e.g., Tsurutani 1985; Ghavamian et al. 2006; Balogh & Treumann 2013).

The counter-streaming protons produced by encountering the electric field result in modifications to the proton particle distributions. Figure 7 shows the vertical component of the electric field from the simulation, and the relative-to-the-line-of-sight instrumentation in Figure 5 shows an analysis of the vertical component of the proton momentum ($p_{z,i} = m_p v_{zi}$) from the 3D simulation shown in previous figures. The top left of the figure shows the magnitude of the vertical component of the proton momentum (a proxy for vertical kinetic energy), against altitude z (in dimensionless units of $c/\omega_{pe} = 1.7$ km for a density of 10×10^6 m^{-3}). Shown below are examples of the proton distribution functions for selected altitudes of $z = 20$, 60, and $100c/\omega_{pe}$. These represent examples of distribution functions that could be expected to be encountered by a spacecraft passing (A) below the magnetopause barrier, (B) just above the barrier, and (C) in the "foot" region upstream of the encounter. The incoming proton stream has a narrow (cold) distribution at -0.04c, and is flowing from right (high z)

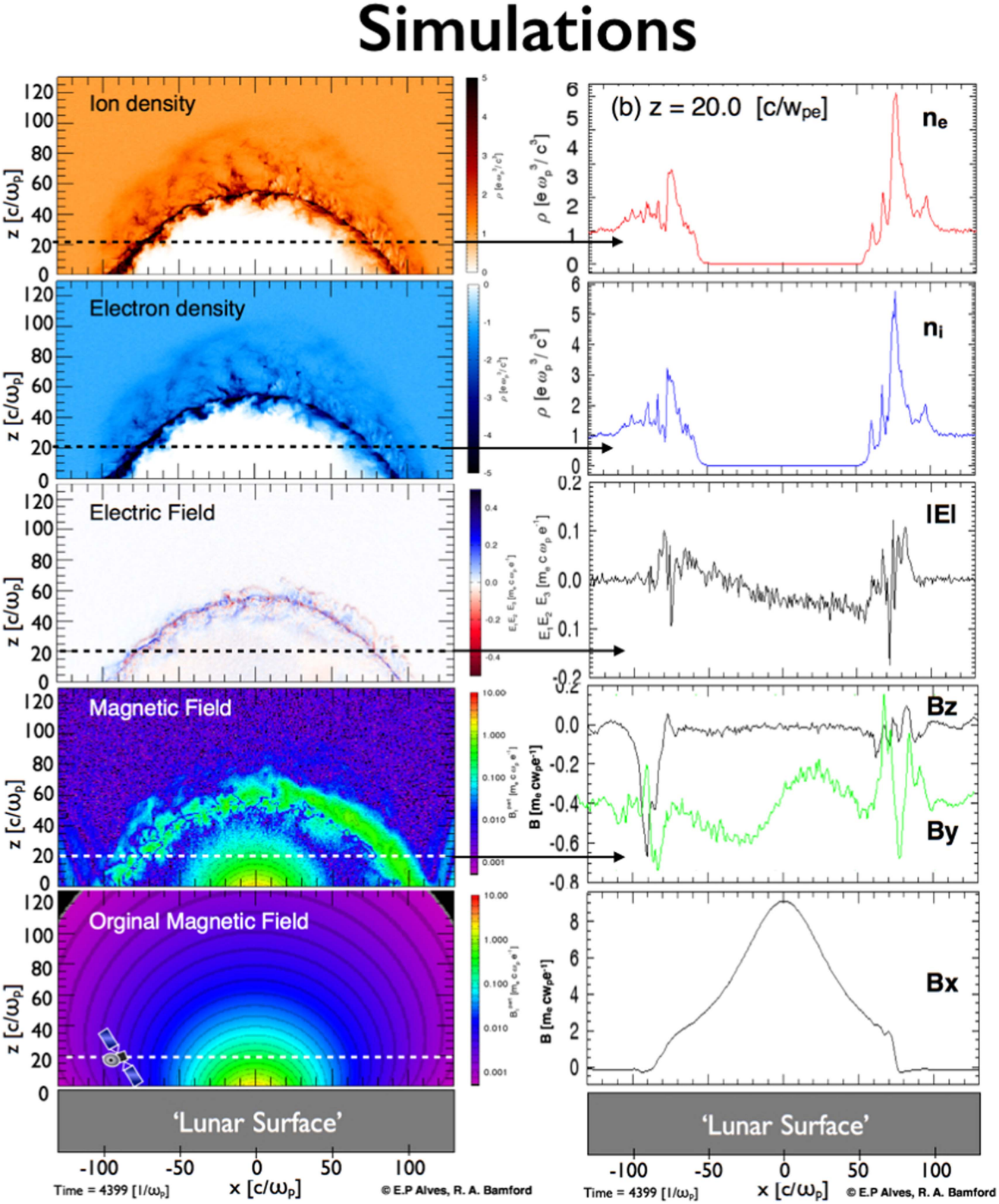

Figure 4. (Left) Planar slices through the 3D simulation shown in Figure 3 showing the behavior of the plasma densities and electromagnetic forces. The location of the plane is indicated in Figure 2. The normalized y-axis represents the altitude above the Moon's surface. The normalized x-axis represents distance along the surface of the Moon, upon which a magnetic dipole field is located. (Right) The simulated spacecraft diagnostic signatures of a transit through a mini-magnetosphere taken from the 3D simulation. The OSIRIS simulation is plotted to recreate the type of signatures that would be observed by spacecraft plasma instrumentation during a flyover of a crustal magnetic anomaly (lower most panel). A low-altitude lunar spacecraft would record in a flyover transit over the surface anomaly at a constant altitude of $h = 5.5 \times c/\omega_{pe}$ in normalized units, the equivalent of ~12 km (for a 5 cm^{-3} density plasma). The simulation is the simplest geometry with a slow wind flow that is normal to the lunar surface; there is no drawn out magnetotail in this example. The simulated data window would be the equivalent of ~2–4 minutes in duration.

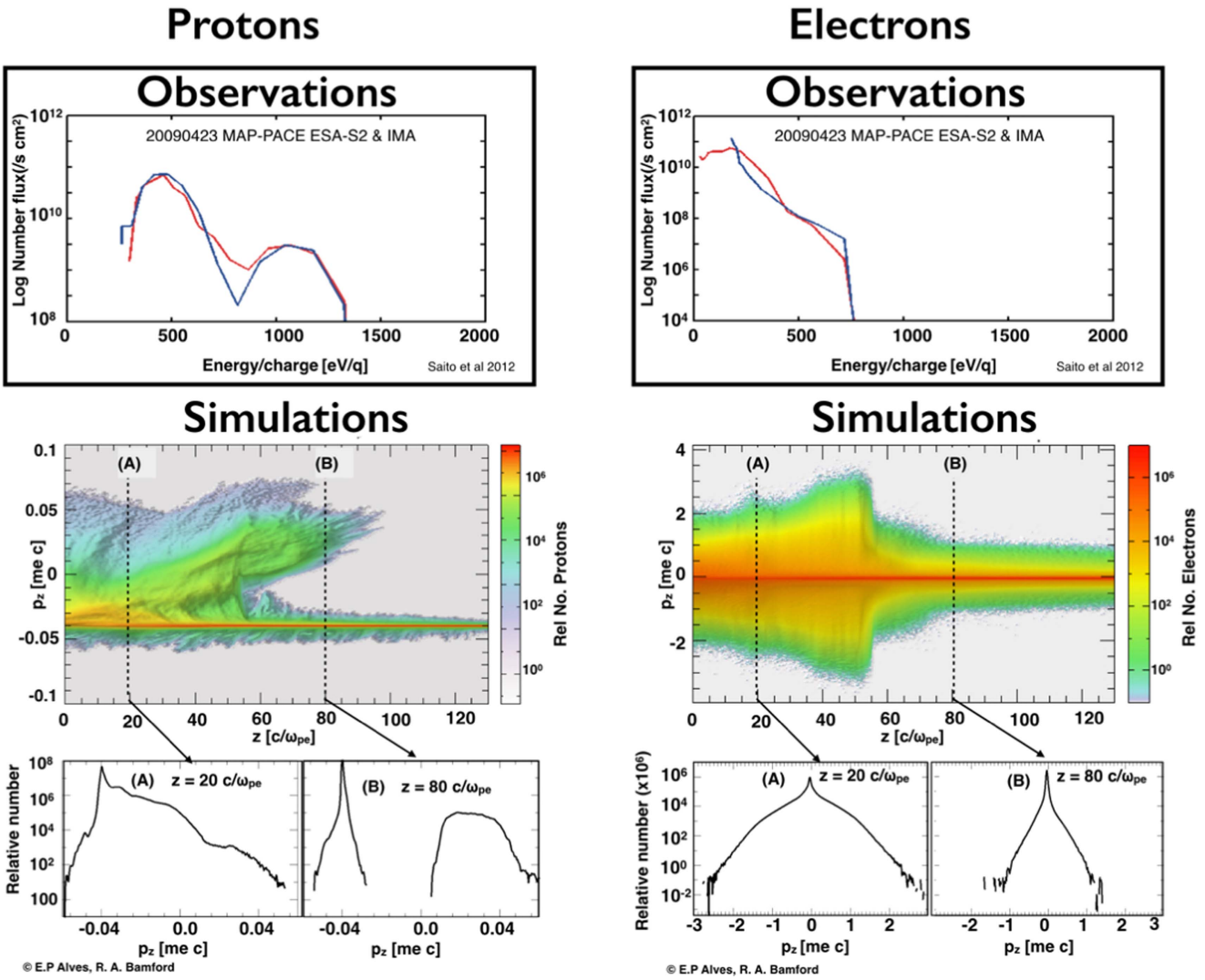

Figure 5. (Left) Protons and (right) electron particle energy spectra comparison. (Top) Observations of the particle energy spectra observed by the *Kaguya* spacecraft at ~25 km altitude (Saito et al. 2012). (Middle and bottom) The vertical component of the particle momentum from the 3D simulation. Below are two examples of the particle momentum distribution spectra at different altitudes from the lunar surface (A) at 20 and (B) 80 c/ω_{pe}. The latter shows the same type of reflected particle distribution seen in the observation example above (top).

to left (low z). As the inflow particles encounter the mini-magnetosphere boundary (at about $z = 55$), the distributions alter. Comparing the form of the distribution functions for the vertical momentum at different altitudes shows the formation of a "bump-on-tail" distribution. The variation with altitude illustrates how observational spectra, such as those observed by non-thermal protons observed by Nozomi (Futaana et al. 2003) at an altitude of 2800 km, are consistent with the simulation and the different spectra observed at lower altitudes, an example of which is shown in the insert labeled (b) "Observations" in Figure 5 (from Saito et al. 2012). A similar comparison can be seen in Figure 5(right) for the electrons. The widening of the vertical momentum component seen in the simulation plot (lower panel) coincides with encountering the barrier region and corresponds to a temperature increase. Together the proton and electron spectra in Figure 5 show that the non-adiabatic exchanges between the particle species are present in both observations and simulations.

The level of detail in the momentum spectra is indicative of the ability of the fully self-consistent simulation code to represent the kinetic instabilities. These can be seen in the periodic structures (such as those seen at $p_z < -0.05$). The "finger-like" structures in the counter-streaming populations, $z > 60$–120 and $p_z > 0.0$–0.05, are indications of waves formed as a result of the modified two-stream instability (Dieckmann et al. 2006; Bingham et al. 2010). These results are also seen in PIC simulations of collisionless shocks of planetary magnetospheres (for example, see Forslund & Freidberg 1971; Forslund et al. 1984; Blandford & Eichler 1987; Quest 1988; Kucharek & Scholer 1995).

4.4. Comparison with Lunar Swirls

A complicated magnetic footprint that is limited in extent and isolated was observed by the SARA instument on *Chandrayaan-1* (Wieser et al. 2010; Vorburger et al. 2012; Futaana et al. 2013) (at 22° S and 240° E on the lunar far side, and shown in the left two panels of Figure 6). Such a structure would appear in the far-field as a single dipole, similar to that used in the simulation (shown in the right panels of Figure 6). The simulation reproduces a wider enhanced ring region about

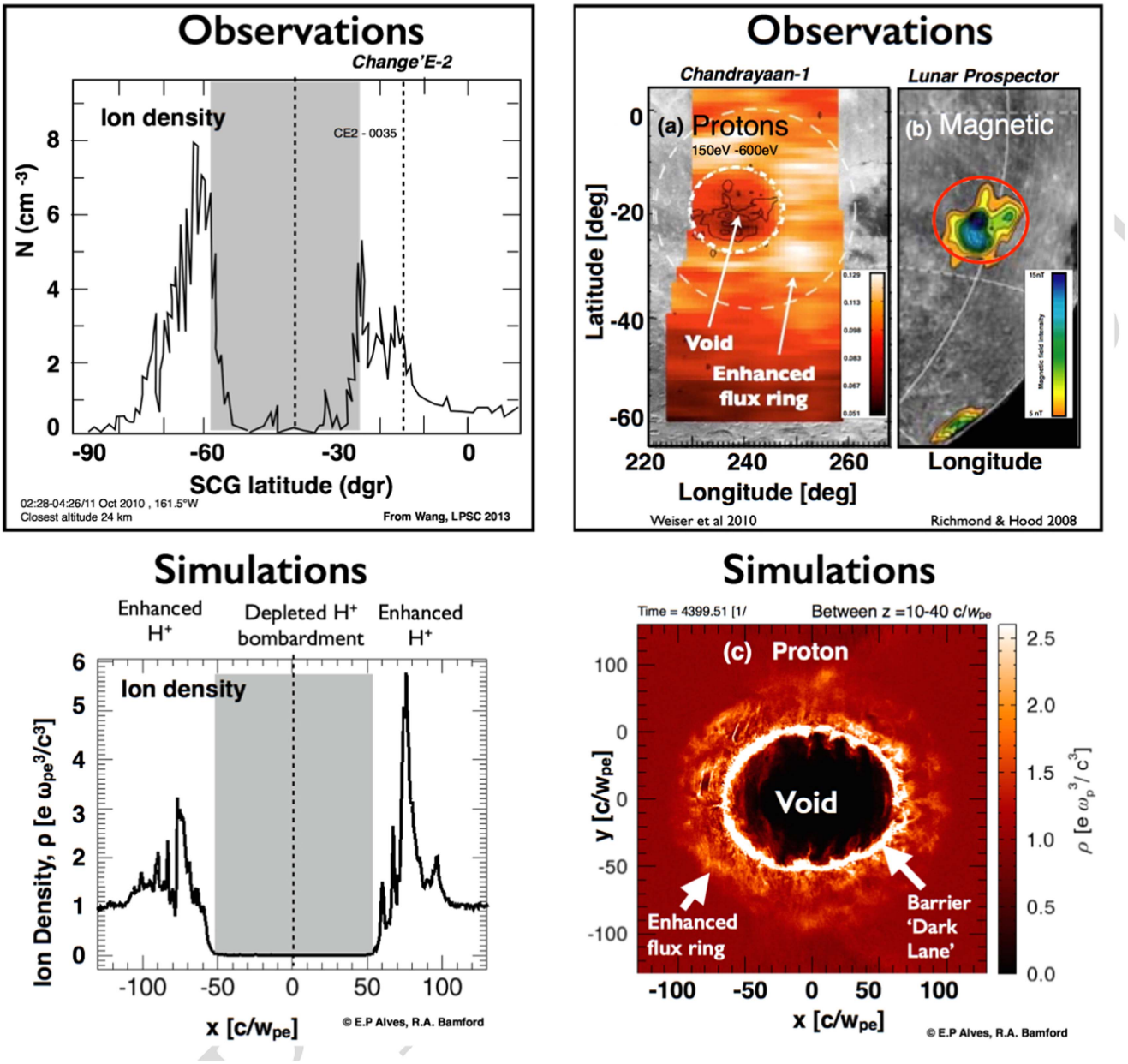

Figure 6. Comparison of simulated and observed proton density. (Left) Top: proton density as a function of SCG latitude obtained from ChangeE-2 lunar orbits. The region encompass the extension of the Serenitatis antipode magnetic anomaly from Wang et al. (2012). Bottom: the simulated relative proton deposition onto the surface of the Moon. (Right) Top: (a) observational data from the Gerasimovich magnetic anomaly showing the spatial variation in energetic neutral hydrogen flux from the surface over the magnetic anomaly near 22° S and 240° E on the lunar far side, observed from 200 km altitude on 2009 June 17 (in unit-less reflection coefficients) from Wieser et al. (2010). (b) A map of the total magnetic field at an altitude of 30 km plotted using a Lambert equal-area projection obtained from *Lunar Prospector* data from Richmond & Hood (2008). Bottom: the stacked relative proton density from above from the 3D simulation (cap excluded).

the central void in the relative proton density spatial distribution in the vicinity of the dipole magnetic field. The static instance and higher resolution of the simulation, compared to the observation, allows the narrow electron-scale barrier and wider pre-transition region to be distinguished. The density variations due to kinetic-scale instabilities and turbulence are also resolved for a moment frozen in time. In space the variations in space weather conditions would randomize, widen, and reduce, as well as introduce asymmetries to the proton spatial distribution. Nevertheless, the simulation illustrates the principles at play and indicates that the determining force controlling the protons is the pondermotive (or energy density gradient) force.

4.5. Simulated Relative Proton flux with Dark Lanes and Lunar Swirls

The relative proton density from the simulation can be further clarified by examining a linear plot taken at the equivalent lunar surface level. This is shown in Figure 6.

If sustained long-term, this pattern of excluded and narrow enhanced proton density, resulting from the action of the mini-magnetosphere with the crustal magnetic field, would be consistent with the distribution and finesse required to form the variety of lighter and darker albedo alterations seen in lunar swirls (Harnett & Kramer 2015).

The relative deposition of proton flux (shown in gray) on the surface slice from the simulation is shown in the image of

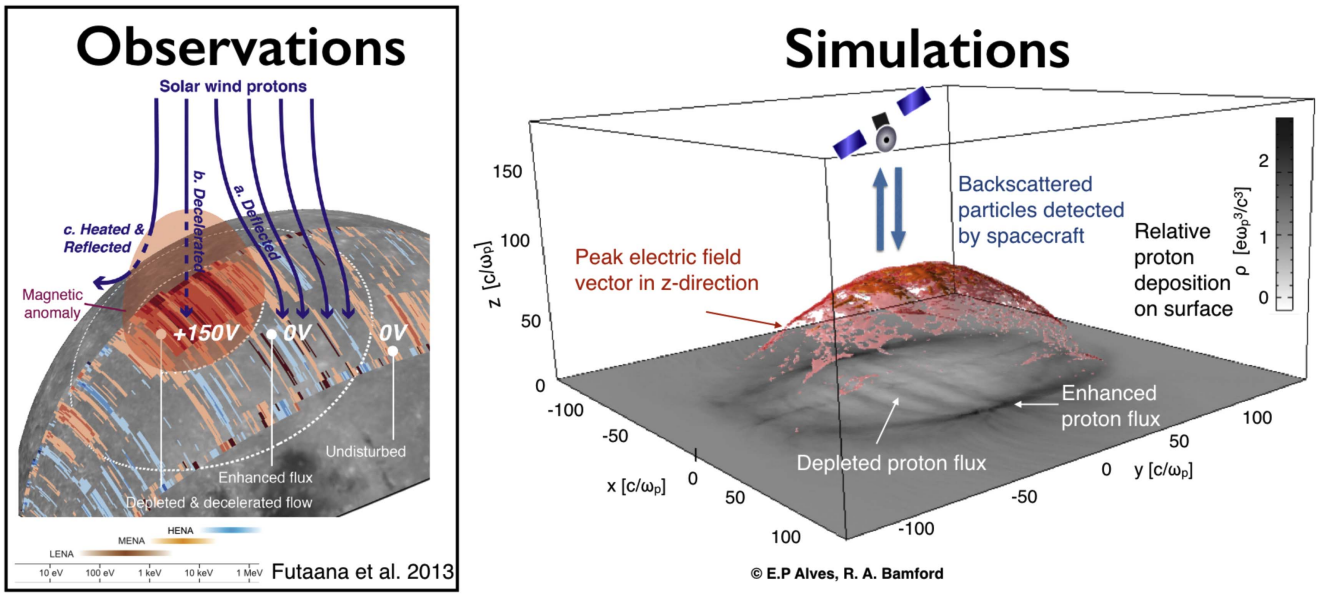

Figure 7. (Left) Observational data showing a 2D map projection onto the lunar surface of the concentration of the electric field potential coincident with the magnetic field of the small isolated anomaly near the Gerasimovich crater on the lunar far side. The observational data were obtained from back-scattered proton flux observed by the ENA instrument on *Chandryaan-1* (Futaana et al. 2013). (Right) Results from the 3D simulation showing the peak electric field vector in the z direction only (red; background values are made transparent for clarity). This component of the electric field will provide the source of the majority of the the back-scattered protons collected by a spacecraft observing from above, with its instrumentation pointing toward the lunar surface. For a density of $n = 10\ \mathrm{cm}^{-3}$ the value of the simulated electric field $\delta E \approx 300$ V.

Figure 8 with the magnetic field lines of the dipole. This is compared to an image of the central region of the most distinctive example of a lunar swirl, the Reiner Gamma Formation located at 7°.4 N, 300°.9 E, taken by NASA's *Lunar Reconnaissance Orbiter* (lroc.sese.asu.edu/posts/575). The agreement between the key characteristics of dark-lane (Bell & Hawke 1982) width and shielded interior can be seen to be totally consistent.

We will now perform a series of simulations to study the parameter regime of single dipoles by varying the orientation and some of the plasma conditions.

5. PARAMETRIC ANALYSIS (USING 2D SIMULATIONS)

In the following section a brief exploration of how: (a) dipole orientation relative to the lunar surface, (b) environmental plasma Alfvén Mach number and parallel or anti-parallel, (c) changes in the surface dipole effective magnetic field intensity and range, affect the results of the simulation and hence the observed signatures. As the parametric analysis shown here is only intended to provide an indication of the relative significance of major parameter changes, a 2D simulation is sufficient.

5.1. The Effect of Dipole Orientation

Changing the orientation of the emerging magnetic dipole relative to the surface plane produces the same diamagnetic characteristics of narrow barrier, particle reflection, cavity formation, waves, and turbulence. However, as can be seen in Figure 9, the overall morphologies of the relative proton distribution are very different.

Figure 9(a) shows 2D simulations of the same magnetic dipole in three orthogonal directions $\boldsymbol{x}$, $\boldsymbol{y}$, and $\boldsymbol{z}$, relative to the surface plane. The solar wind, mass ratio, and plasma conditions are the same as those of the 3D simulation, with the exception that the solar wind has no magnetic field. The consequence of $\boldsymbol{B}_{\rm sw}$ parallel or anti-parallel to the surface magnetic field is shown in the next section.

5.2. The Effects of Changes in the Environmental Plasma

Although the crustal magnetic anomalies are a fixed magnetic field source, the plasma environment is not. There are periodicities due to orbits and diverse solar wind and/or magnetospheric conditions. Through simulations this can be explored in Figures 9(b) and (c).

A qualitative comparison of the variation of mini-magnetosphere characteristics in Figure 9(b) shows that an anti-parallel field creates larger cavities and that the width turbulent layer varies considerably, as does the proton pickup. The higher magnetosonic Mach number that compresses the turbulence region sharpens up the transition and reduces the cavity size. The comparison also illustrates how a spacecraft passing at the same altitude will observe very different conditions. A more oblique angle for the direction of the plasma flow will also multiply the number of combinations that could be recorded for the same magnetic field source.

A spacecraft passing over the vicinity of these anomalies, at a fixed height (as indicated in the figures by a satellite graphic and dashed "flight-path" line) but under different plasma conditions, will sometimes transect the different regions of a mini-magnetosphere and thus observe different characteristics. (An illustration of these plasma data instrumentation signatures in such a flyover is shown in Figure 4).

Figure 9(b) illustrates the consequence of combinations of changes in the simulation conditions. In Figure 9(a), the incoming solar wind magnetosonic mach numbers M_m and parallel (or anti-parallel) solar wind magnetic field $\boldsymbol{B}_{\rm sw}$ orientations are varied. In Figure 9(c) the dipole size/length, $L_{\rm dipole}$, is altered. The extent of the dipole can be altered either through being a larger single crustal magnetic field or by

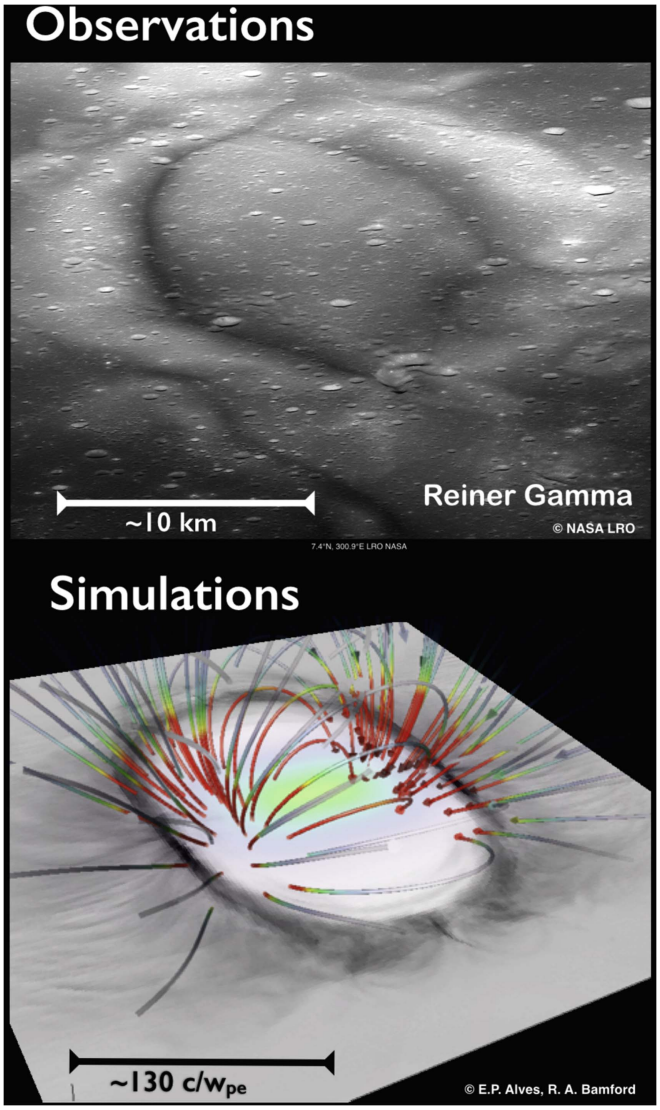

Figure 8. Top: image of the central region of the Reiner Gamma Formation lunar swirl taken by NASA's *Lunar Reconnaissance Orbiter* (lroc.sese.asu.edu/posts/575). Bottom: a slice of the relative proton density from the 3D simulation, with the initial magnetic field lines from a single subsurface dipole. The grayscale distribution is darker for higher densities of protons, and whiter for lower densities. The form and relative width of the "dark lanes" (Bell & Hawke 1982) suggest that the aspect ratio of dark-lane width to cavity width is similar in both cases.

multiple smaller conglomerations (such as on the far side of the Moon) that will appear as a single dipole when observed in sufficient altitude to be in the far-field. If two regions of magnetic anomalies are sufficiently far apart then they will appear as two dipoles and so on. The complexity of the near-field, ground-level magnetic topology cannot readily be identified from space, due to the interaction of the original magnetic field and the environmental plasma that is creating in situ currents, electric fields, and compensating local magnetic variations at or near the altitude of the spacecraft flyover. For this reason, simulating a distribution of magnetic dipoles over the surface can provide equally valid answers.

In all these figures the white-to-red color distribution represents relative proton density and all the conditions are the same except for those stated as otherwise.

In summary, the 2D simulations show how, occasionally, certain features like the diamagnetic cavity might be clearly detected in in situ instrumentation, such as particle detectors and magnetometers. This is especially true for a rapid spacecraft transit through very small isolated magnetic field anomalies. However, other instruments such as imagers (Wieser et al. 2010), that look down onto the features, could still detect the characteristic depletion in proton reflection.

6. CONCLUSIONS

In this paper, for the first time, the results from a fully self-consistent 3D PIC simulation are shown side-by-side with in situ observations from several lunar satellites investigating lunar magnetic anomalies. The conditions used in the PIC simulation are consistent with actual conditions. These simulations show that a magnetic field intensity of $<300nT$ is sufficient to produce a "mini-magnetosphere" with a collisionless shock and diamagnetic cavity, for a solar wind density of 10 cm^{-3}, with a $10nT$ interplanetary magnetic field, flowing at 600 km s^{-1}—a magnetosonic Mach number of 8.

We have demonstrated, for the first time, that collisionless shocks can form at sub-proton Larmor orbit dimensions.

All of the observational characteristics identified as being associated with lunar mini-magnetospheres are accounted for in the comparison. This includes, in particular, the origin of the dark lanes of the lunar swirls, in agreement with the spectroscopic observations of lunar surface albedo (Pieters et al. 1993; Taylor et al. 2001; Blewett et al. 2007; Kramer et al. 2011a, 2011b; Glotch et al. 2015). The in situ observations from plasma instrumentation on board satellites at altitudes from 10–1000 s km include; magnetic and density pile-up, backflow, narrow electrostatic barrier, solitary and lower-hybrid waves, turbulence spectrum, Whistlers, cavity formation, beams, particle pickup, electron heating, ion-slowing, reflection and deflection. The 3D simulation has reproduced all these using the simplest of magnetic topologies —a single magnetic dipole. The single dipole represents an archetype. It can be a far-field resultant magnetic structure of conglomerations of random surface fields, as well as represent a component part of a more complicated distributed near-field surface magnetic field topology.

It is shown in this paper that different orientations and plasma conditions alter the archetype. The magnetic fields simulated are modest, hundreds of nT for realistic solar wind flow velocities ~100s km s^{-1}, densities ~1–100 cm^{-3}, plasma β <1, realistic charge-to-mass ratios, and Alfvèn Mach numbers of 2–8.

In all orientations, a narrow electrostatic field forms at the locations where the magnetic field and particle densities pile-up. The magnitude of the electrostatic field is proportional to the *gradient* in magnetic field in accordance with theory and laboratory experiments (Bamford et al. 2012). This occurs as a result of the impacting plasma environments (the solar wind plasma and the plasma in and immediately around the fixed footprint of the surface magnetic field). The thickness of this barrier is approximately equal to the electron skin depth c/ω_{pe} (where ω_{pe} is the electron plasma frequency) in agreement with theory for collisionless shocks (Tidman & Krall 1971).

The 3D simulation was of a dipole whose magnetic axis was parallel to the surface but buried below it. Because it was 3D it showed how the outwardly pointing, narrow electrostatic field formed in every orientation, resulting in a protective "dome"

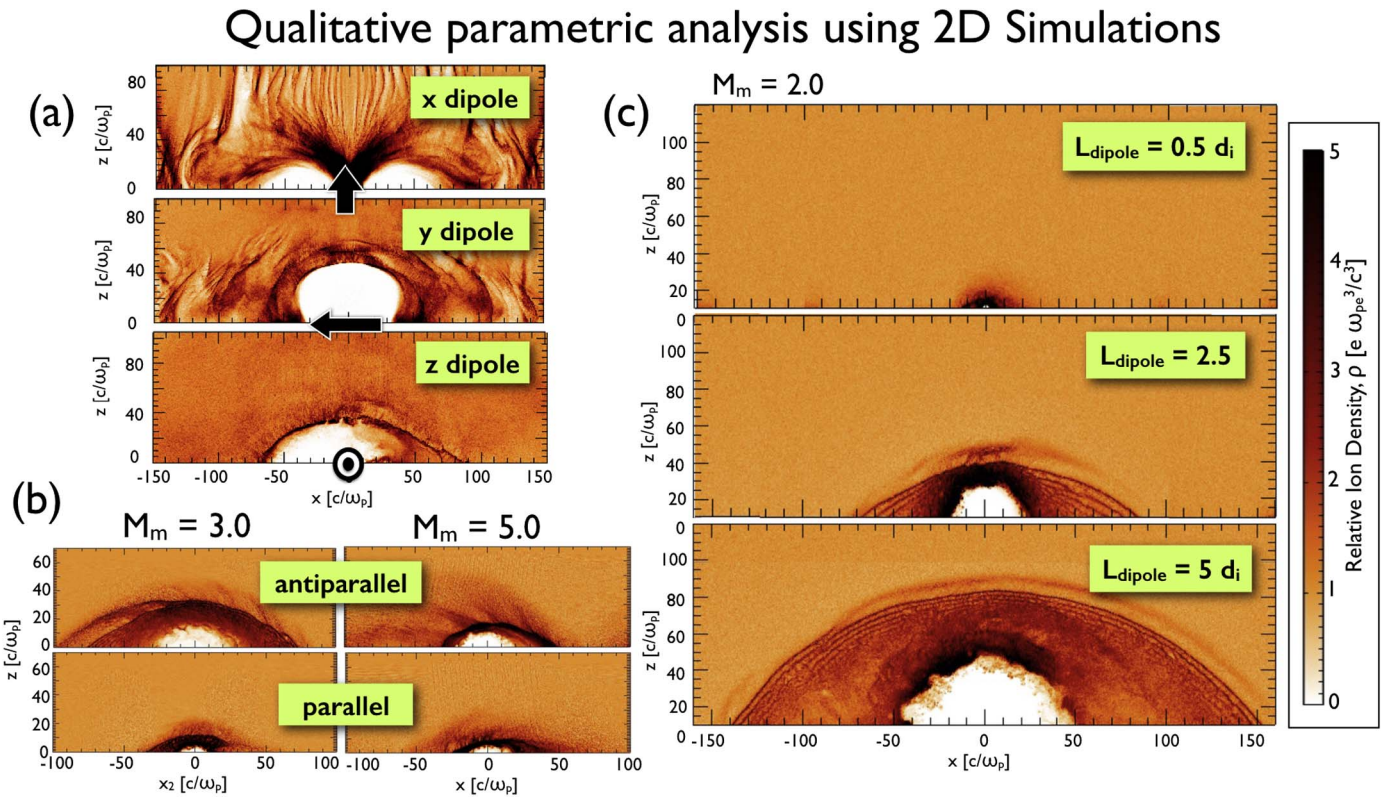

Figure 9. A qualitative parametric analysis using 2D Simulations. (a) Different orientations of magnetic dipole axis aligned in the *x, y, z* direction. The vertical, *x*, dipole orientation (top) shows the converging particle deposition of an auroral-like structure. $M_{\rm m} = 8$ and $m_p/m_e = 1836$. (b) Changes in incoming plasma flow speed and magnetic field for parallel and anti-parallel field conditions. Perpendicular shocks by cold plasma with fixed dipole size/strength ($L_{\rm dipole} = 2$), varying magnetosonic Mach number, $M_m = 3, 5$, for parallel (bottom) and anti-parallel (top) $B_{\rm dipole}$. Reduced 2D parameters: the incoming flow velocity is ×50, a typical solar wind speed, the proton-to-electron mass ratio m_p/m_e is $\sim 1/20$, a realistic value, chosen for computational speed. (c) Changes to surface dipole magnitude and range. Perpendicular shocks by cold plasma with fixed magnetosonic Mach number $M_{\rm m} = 2.0$, with $B_{\rm in}$ parallel to $B_{\rm dipole}$, with varying dipole size/strength $L_{\rm dipole} = 0.5, 2.5, 5$.

that scattered the incoming protons, thereby reducing the proton flux that reached the lunar surface. The dome was compressed by the solar wind pressure, resulting in a spreading of the dipole mid-plane, parallel to the surface magnetic field lines. At the edges of the dome, the narrow, electrostatic sheath intersected the lunar surface, producing a means of channeling a higher proportion of the impacting proton flux into narrow regions or "lanes" around the edge of the protected dome. The widths of these enhanced proton outlines are of the order of the electron dynamics (a kilometer or less) and resembles, in form and width, the "dark lanes" of the lunar swirls. Similar electron-scale plasma filamentations occurred at the poles—which were laid horizontally in the 3D example used here.

Together these finding support the hypothesis that the observed spectral effects that result in lunar swirls are due to differential proton bombardment. One prediction of this work is that the dark lanes' widths will be the same for any of the lunar swirls distributed about the Moon, whether they are in large conglomerations or isolated patches.

The authors would like to thank the Science and Technology Facilities Council for fundamental physics and computing resources that were provided by funding from STFC's Scientific Computing Department, and would like to thank the European Research Council (ERC 2010 AdG Grant 267841) and FCT (Portugal) grants SFRH/BD/75558/2010 for support. We acknowledge PRACE for rewarding access to the supercomputing resources SuperMUC and JUQUEEN, based in Germany.

REFERENCES

Acuna, M., Connerney, J., Lin, R., et al. 1999, Sci, 284, 790
Balogh, A., & Treumann, R. A. 2013, Physics of Collisionless Shocks: Space Plasma Shock Waves (Berlin: Springer)
Bamford, R., Alves, E., Cruz, F., et al. 2015, arXiv:1505.06304v1
Bamford, R., Alves, E., Kellett, B., et al. 2013a, LPICo, 1719, 1292
Bamford, R., Alves, E., Kellett, B., et al. 2013b, in European Planetary Science Congress, 8, 542
Bamford, R., Gibson, K., Thornton, A., et al. 2008, PPCF, 50, 124025
Bamford, R., Kellett, B., Bradford, W., et al. 2012, PhRvL, 109, 81101
Bell, J. F., & Hawke, B. R. 1982, LPSC, 12, 679
Bell, J. F., & Hawke, B. R. 1987, PASP, 99, 862
Bingham, R. 1993, in Plasma Physics: An Introductory, ed. R. Dendy, (Cambridge: Cambridge Univ. Press)
Bingham, R., Bamford, R., Kellett, B., & Shapiro, V. 2010, JPlPh, 76, 915
Blandford, R., & Eichler, D. 1987, PhR, 154, 1
Blewett, D., Hawke, B., Richmond, N., & Hughes, C. 2007, GeoRL, 34, L24206
Blewett, D. T., Hawke, B. R., Richmond, N. C., et al. 2011, JGR, 116, 1
Borisov, N., & Mall, U. 2003, PhLA, 309, 277
Coleman, P., Lichtenstein, B., Russell, C., Sharp, L., & Schubert, G. 1972, GeCoA, 36, 2271
Connor, J. 1988, PPCF, 30, 619
Cruz, F., Alves, E., Bamford, R., et al. 2015, in 42nd EPS Conf. on Plasma Physics, 408
Cruz, F., Alves, E., Bamford, R., et al. 2016, APS Division of Plasma Physics Meeting, 12.121
Dawson, J. M. 1983, RvMP, 55, 403
Deca, J., Divin, A., Lapenta, G., et al. 2014, PhRvL, 112, 151102

Deca, J., Divin, B., Lembège, A., et al. 2015, JGRA, 120, 6443
Dieckmann, M. E., Eliasson, B., Shukla, P. K., Sircombe, N. J., & Dendy, R. O. 2006, PPCF, 48, B303
Dyadechkin, S., Kallio, E., & Wurz, P. 2015, JGRA, 120, 1589
Dyal, P., Parkin, C. W., & Sonett, C. P. 1970, Sci, 169, 762
Edberg, N. J., Lester, M., Cowley, S., et al. 2010, JGRA, 115, 7203
El-Baz, F. 1972, LPSC, 3, 39
El-Baz, F., Worden, A., & Brand, V. 1972, LPSC, 3, 219
Fatemi, S., Lue, C., Holmström, M., et al. 2015, JGRA, 120, 4719
Fonseca, R., Silva, L., Tsung, F., et al. 2002, LNCS, 2331, 342
Forslund, D., & Freidberg, J. 1971, PhRvL, 27, 1189
Forslund, D., Quest, K., Brackbill, J., & Lee, K. 1984, JGRA, 89, 2142
Futaana, Y., Barabash, S., Wieser, M., et al. 2010, JGR, 115, A10248
Futaana, Y., Barabash, S., Wieser, M., et al. 2013, GeoRL, 40, 262
Futaana, Y., Machida, S., Saito, Y., Matsuoka, A., & Hayakawa, H. 2003, JGR, 108, 1025
Gargaté, L., Bingham, R., Fonseca, R., et al. 2008, PPCF, 50, 074017
Garrick-Bethell, I., Head, J. W., & Pieters, C. M. 2011, Icar, 212, 480
Ghavamian, P., Laming, J. M., & Rakowski, C. E. 2006, ApJL, 654, L69
Glotch, T. D., Bandfield, J. L., Lucey, P. G., et al. 2015, NatCo, 6, 6189
Halekas, J., Brain, D., Mitchell, D., & Lin, R. 2006, GeoRL, 33, 22
Halekas, J., Mitchell, D., Lin, R., et al. 2001, JGRE, 106, 27
Halekas, J., Poppe, A., McFadden, J., et al. 2014, GeoRL, 41, 7436
Harnett, E., Kramer, G., Udovicic, C., & Bamford, R. 2016, arXiv:1605.05778
Harnett, E. M., & Winglee, R. M. 2002, JGR, 107, 1421
Harnett, E. M., & Winglee, R. M. 2003, JGR, 108, 1088
Hashimoto, K., Hashitani, M., Kasahara, Y., et al. 2010, GeoRL, 37, L19204
Hood, L., & Schubert, G. 1980, Sci, 208, 49
Hood, L., & Williams, C. 1989, LPSC, 19, 99
Hood, L. L., & Artemieva, N. A. 2008, Icar, 193, 485
Huixian, S., Shuwu, D., Jianfeng, Y., Ji, W., & Jingshan, J. 2005, JESS, 114, 789
Jarvinen, R., Alho, M., Kallio, E., et al. 2014, GeoRL, 41, 2243
Kallio, E., Jarvinen, R., Dyadechkin, S., et al. 2012, P&SS, 72, 146
Kato, M., Sasaki, S., & Takizawa, Y. 2010, SSRv, 154, 3
Kivelson, M., Wang, Z., Joy, S., et al. 1995, AdSpR, 16, 59
Kramer, G. Y., Besse, S., Dhingra, D., et al. 2011a, JGR, 116, E00G18
Kramer, G. Y., Combe, J.-P., Harnett, E. M., et al. 2011b, JGR, 116, E04008
Kucharek, H., & Scholer, M. 1995, AdSpR, 15, 171
Kurata, M., Tsunakawa, H., Saito, Y., et al. 2005, GeoRL, 32, 24
Lacina, J. 1971, PlPh, 13, 303
Langmuir, I. 1929, PhRv, 33, 954
Lin, R., Mitchell, D., Curtis, D., et al. 1998, Sci, 281, 1480
Lue, C., Futaana, Y., Barabash, S., et al. 2011, GeoRL, 38, L03202
Lyon, E. F., Bridge, H. S., & Binsack, J. H. 1967, JGR, 72, 6113
McBride, J. B., Ott, E., Boris, J. P., & Orens, J. H. 1972, PhFl, 15, 2367
Nakagawa, T., Takahashi, F., Tsunakawa, H., et al. 2011, EP&S, 63, 37
Pieters, C., Fischer, E., Rode, O., & Basu, A. 1993, JGRE, 98, 20817
Pinet, P. C., Shevchenko, V. V., Chevrel, S. D., Daydou, Y., & Rosemberg, C. 2000, JGRE, 105, 9457
Poppe, A., Halekas, J., Delory, G., & Farrell, W. 2012, JGRA, 117, 9105
Quest, K. 1988, JGRA, 93, 9649
Richmond, N., & Hood, L. 2008, JGR, 113, E02010
Richmond, N., Hood, L., Halekas, J., et al. 2003, GeoRL, 30, 1395
Ryutov, D., Drake, R., & Remington, B. 2000, ApJS, 127, 465
Saito, Y., Nishino, M. N., Fujimoto, M., et al. 2012, EP&S, 64, 83
Schultz, P. H., Srnka, L. J., Pai, S., & Menon, S. 1980, LPSC, 11, 1009
Starukhina, L. V., & Shkuratov, Y. G. 2004, Icar, 167, 136
Taylor, L. A., Pieters, C. M., Keller, L. P., Morris, R. V., & McKay, D. S. 2001, JGRE, 106, 27985
Tidman, D., & Krall, N. A. 1971, in Shock Waves in Collisionless Plasmas, ed. S. C. Brown, (New York: Wiley)
Tsurutani, B. T. 1985, Collisionless Shocks in the Heliosphere: Reviews of Current Research (Washington, DC: American Geophysical Union)
Vorburger, A., Wurz, P., Barabash, S., et al. 2012, JGR, 117, A07208
Wang, X., Horányi, M., & Robertson, S. 2012, JGR, 117, A06226
Wieser, M., Barabash, S., Futaana, Y., et al. 2010, GeoRL, 37, L05103_1
Wieser, M., Barabash, S., Futaana, Y., et al. 2009, P&SS, 57, 2132
Yokota, S., Saito, Y., Asamura, K., et al. 2014, P&SS, 93, 87